

# Experimental and numerical investigations on microstereolithography of ceramics

C. Sun and X. Zhang

*Department of Mechanical and Aerospace Engineering, University of California Los Angeles, Los Angeles, California 90095*

(Received 12 April 2002; accepted for publication 2 July 2002)

Microstereolithography ( $\mu$ SL) uses laser light to solidify UV-curable resin mixed with concentrated ceramic powders. During the  $\mu$ SL process, the light scattering from the particle suspension is found to significantly influence the fabrication resolution in both lateral and depth dimensions which are critical for the complex three-dimensional (3D) microfabrication. In this work, we performed Monte Carlo simulations and experimental studies to understand the detailed microscale optical scattering, chemical reaction (polymerization), and their influence on critical fabrication parameters. As a result, it was found that due to the scattering, the fabricated line is wider in width and smaller in depth compared with polymeric fabrication at the same condition. The doping technique that we used substantially reduced the light scattering, which in turn enhanced the fabrication precision and control. In addition, the experimental values of curing depth and radius agreed reasonably well with the theoretical modeling. When a laser beam was focused to the diffraction limit, an ultimate linewidth resolution with ceramic  $\mu$ SL was found at about 2.6  $\mu$ m. © 2002 American Institute of Physics. [DOI: 10.1063/1.1503410]

## INTRODUCTION

Microelectromechanical systems (MEMS) have made significant progress in the past decade.<sup>1,2</sup> Since the surface micromachining technique was introduced to MEMS, a variety of microfabrication techniques have been developed. Compared with common microfabrication methods, such as silicon micromachining and LIGA (German Lithography, electroforming, and molding), solid microscale freeform fabrication (SFF) possesses unique advantages in building geometrically complex three-dimensional (3D) structures and handling a broad spectrum of functional materials.

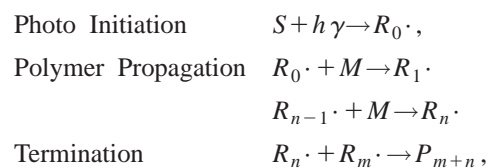
Macroscale SFF can directly fabricate a complex free-standing 3D structure from the computer-aided design (CAD) model. Several SFF methods are known: stereolithography,<sup>3,4</sup> selective laser sintering,<sup>5</sup> fused deposition modeling, sanders prototyping, and 3D printing.<sup>6,7</sup> These methods were originally used to fabricate plastic, wax, and paper models. Recently, they have also been used in direct fabrication of ceramic and metal parts.<sup>5,8,9</sup>

Microstereolithography ( $\mu$ SL) derived from conventional stereolithography, provides the unique opportunity of fabricating complex high-aspect ratio 3D microstructures. This  $\mu$ SL process successfully demonstrates the fabrication of polymer 3D microstructures.<sup>10–12</sup> A two-photon photopolymerization has also been developed to achieve submicron resolution.<sup>13</sup> By using a modified  $\mu$ SL process, assembly-free 3D microstructures can be built.<sup>14</sup>

All these results demonstrate the feasibility of using  $\mu$ SL to fabricate ultrafine 3D polymeric microstructures. However, additional postprocesses, such as electroplating, must be used to fabricate metal parts from the polymer mold.

Recently, direct  $\mu$ SL fabrication of ceramic microstructures has also been successfully developed.<sup>12</sup> This technique

uses ultraviolet (UV) laser light to solidify the UV-curable resin mixed with concentrated ceramic powders (50% vol) (Figure 1). The basic principle of microstereolithography is the space-resolved laser-induced polymerization in the UV curable resin.<sup>3</sup> The UV curable resin is a mixture of monomer, photoinitiator, ceramic powders, and additives such as light absorber. Incoming photons are absorbed by photoinitiator molecules, which are subsequently split into primitive radicals. The radicals react with the monomer molecules to form the reactive polymer chains. These reactive polymer chains in turn propagate with more monomer molecules being added to them. The propagation terminates when two of the reactive polymer chains combine, and therefore, form a nonreactive polymer molecule. The above picture can be generalized as initiation, propagation, and termination, which can be represented by<sup>15</sup>



where  $S$  is photo-initiator,  $h\gamma$  the photon,  $R_0$  the primitive radical,  $M$  the monomer molecules,  $R$  the reactive polymer chains, and  $P$  the polymer molecule. The desired polymerized part can be fabricated by scanning the laser beam according to the CAD model.

During the ceramic  $\mu$ SL fabrication, the laser light scattering from the particle suspension is found to significantly influence the lateral resolution and curing depth, which are critical for forming high-resolution complex 3D microstructures. Figure 2 shows a ceramic disk fabricated by the  $\mu$ SL method. The fabricated disk is 350  $\mu$ m in diameter, which is larger than its designed value of 300  $\mu$ m due to the light

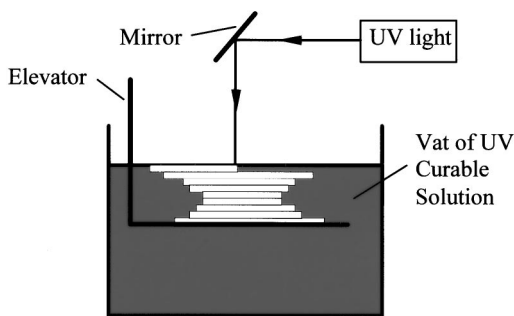


FIG. 1. Schematic diagram of micro stereolithography ( $\mu$ SL).

scattering. In order to effectively reduce the light scattering, a UV doping technique has been developed, whereby UV dopants are introduced into the suspension that strongly absorb the scattered laser light from ceramic particles.<sup>16</sup>

In this system, 1,6-hexanedioldiacrylate (HDDA,  $[H_2C=CHCO_2(CH_2)_3-]_2$ ) is used as a monomer and benzoin ethyl ether [BEE,  $C_6H_5CH(OC_2H_5)COC_6H_5$ ] as a photoinitiator. The typical absorption coefficient in BEE at 364 nm is  $\epsilon_{BEE} = 20 \text{ m}^2/\text{mol}$ . The UV dopant we added into the resin is Tinuvin 324 commercialized by Ciba; its absorption coefficient at 364 nm is  $\epsilon_{Tinuvin} = 2.0 \times 10^4 \text{ m}^2/\text{mol}$ , which is 1000 times higher than the BEE.

In order to examine the doping effect in the  $\mu$ SL of ceramic, four suspensions with UV dopants are prepared with doping levels of 0%, 0.1%, 0.2%, and 0.3%. Disks with the same design dimensions are fabricated at these four doping levels. It has been observed that with increased doping, the diameter of the disk is reduced and approaches the designed value (Table I). These results demonstrate that the optical doping could provide an effective solution to reduce the scattering and enhance the fabrication resolution.

Understanding fundamental physics of scattering and photochemistry involved in ceramic  $\mu$ SL is important for the optimization of the fabrication. Unfortunately, there is no analytic solution available to describe the multiple light scattering from small particles with diameter in the order of the wavelength of the light.<sup>17</sup> A modified Beers law was developed to study how the light scattering influenced curing depth by examining the square of the refractive indexes differences between the ceramic and the medium refractive indexes.<sup>18</sup> But this does not explain how the light scattering

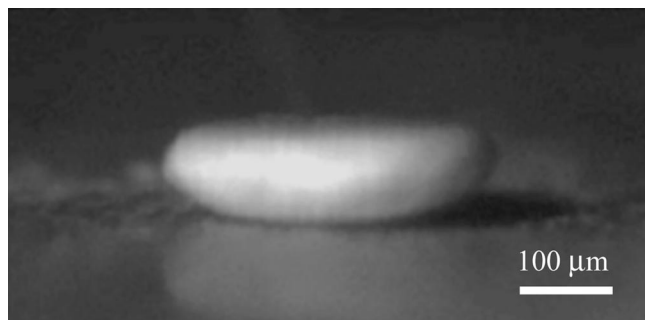


FIG. 2. Ceramic disk (350  $\mu$ m in diameter) fabricated on silicon substrate by  $\mu$ SL method with the designed size of 300  $\mu$ m.

TABLE I. Disk experiment with different UV doping concentrations.

UV absorber	Designed size ( $\mu$ m)	Fabricated size ( $\mu$ m)
0%	500	600 $\pm$ 10
0.1%	500	600 $\pm$ 10
0.2%	500	540 $\pm$ 10
0.3%	500	500 $\pm$ 10

influences the lateral resolution and the shape of the solidified parts.

Liao and Coyle used the Kubelka-Munk (KM) theory to study the multiple light scattering.<sup>19</sup> The KM theory simplifies the radiation fields into forward and backward radiation fluxes. Yet, this theory does not explain the geometrical distribution of the scattered light.

In this particular study, a Monte Carlo ray-tracing technique has been developed not only to investigate the light-scattering effect on  $\mu$ SL of ceramic, but also to overcome the above limitations in using theoretical models (Fig. 3). Though photon scattering by a single particle has been determined by the Mie theory, the Monte Carlo technique goes a step further.<sup>16</sup> Once an optical profile of the light scattering in suspension has been obtained from Monte Carlo simulation, the detailed microscale photopolymerization is numerically simulated. This simulation includes optical absorption, light scattering, photoinitiation, and polymerization kinetics, and is carried out by the finite difference method. This simulation is carefully designed in order to verify the theoretical modeling. And, in order to elucidate important physical mechanisms in the complicated processes, the light scattering and doping effects in  $\mu$ SL of concentrated ceramic suspensions are experimentally investigated.

**NUMERICAL MODELING**

As shown in Fig. 4, the numerical model consists of two major parts: light scattering and photopolymerization.

**A. Light scattering**

The Monte Carlo ray-tracing technique is applied to simulate the multiple light scattering on a ray-by-ray basis.<sup>20</sup>

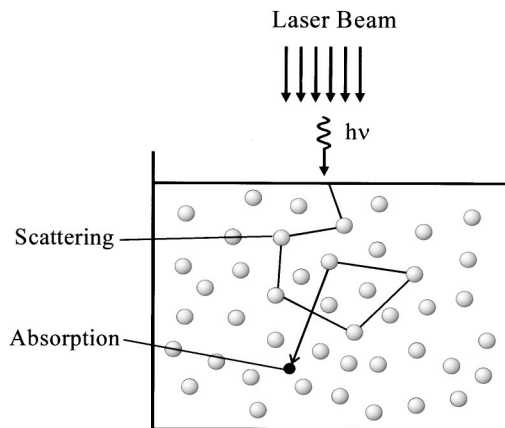
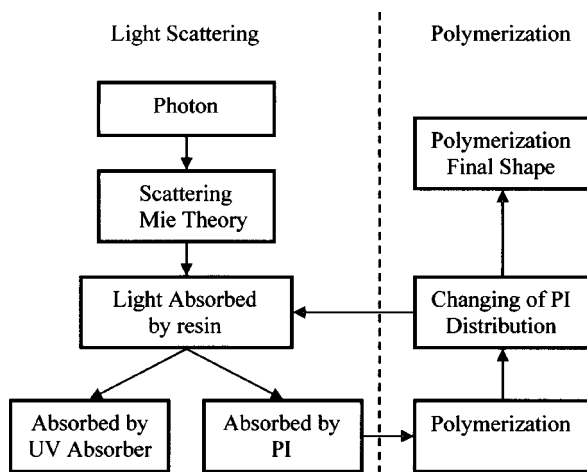


FIG. 3. Physical mechanisms in microstereolithography of concentrated ceramic suspensions: Optical scattering, absorption, and photopolymerization.

FIG. 4. Flow chart of the numerical simulation of ceramic  $\mu$ SL.

The computation of the light scattered by particles consists of generating, traveling, scattering, and absorbing of the photons. The method is formulated in the following sections with the emphasis on derivation of the probability density functions (PDF) used for sampling the critical variables of each computational step.

### 1. Generation of the photon packets

A simple variance reduction technique is used to improve the efficiency of the Monte Carlo simulation. This technique permits equivalently propagating of multiple photons as a single packet along a particular pathway simultaneously. Photon packets are statistically generated according to the characteristics of the laser beam. In this particular case, photons are generated above the surface of the ceramic suspension. Each photon is vertically shot into the ceramic suspension. Because the incident laser beam is a Gaussian beam, the PDF of photon generation is determined by the Gaussian distribution

$$p(x) = e^{-x^2/w_0^2}. \quad (1)$$

This is defined where  $x$  is the location of generated photon, and  $w_0$  is the Gaussian radius of incident laser beam.

### 2. Photon traveling before scattered by ceramic particles

After the photon is shot into the ceramic suspension, it travels through a certain distance  $l$  before it hits a ceramic particle. The probability ( $p$ ) of the scattered photon that can travel further than a given length  $l$  is described by the exponential distribution

$$p(l) = e^{-l/\lambda}, \quad (2)$$

where  $\lambda$  is the mean free path (MFP) of the photons. The MFP is determined by both radius ( $r$ ) of the ceramic particles as well as solid loading or volume ratio ( $s$ ) of the ceramic particles in the suspension

$$\lambda = \frac{4r}{3s}.$$

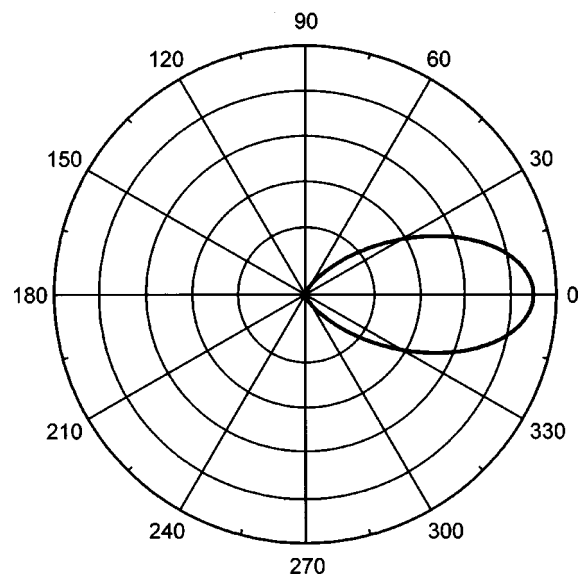


FIG. 5. Normalized intensity profile of light scattered by a single spherical particle embedded in the UV curable resin can be calculated using the Mie theory. The incident light is propagating along the horizontal direction and illuminates the spherical particle located at the center. The diameter of the particle is  $0.5 \mu\text{m}$ . The refractive index of particle and UV curable resin are 1.7 and 1.4, respectively.

To simplify the simulation, we assume all the ceramic particles have uniform radii. Thus, the PDF of travel distance is determined by Eq. (2) with the given particle radius  $r$  and the solid loading  $s$ .

### 3. Photon scattering by ceramic particles

Once the photon hits the particle, it is scattered by the particle. Analytic solution of photon scattering by a single particle can be solved by applying the Mie theory.<sup>16</sup> The distribution of scattered light solved by the Mie theory is used as the PDF for sampling the scattering direction during the computation. The incident photon on the particle is assumed to be at the center. A typical light-scattering pattern shown in Fig. 5 is simulated by applying specific material properties while in the simulation, the scattering pattern needs to be calculated when the material properties are changed.

### 4. Absorption of photons

While photons travel through the monomer media from one particle to another, there is a certain probability of them being absorbed by either photo-initiators or UV. The PDF of the absorption is described by the classical Beers law

$$p_a = 1 - e^{-\varepsilon l} = 1 - e^{-\varepsilon_{PI}l} e^{-\varepsilon_{UV}l},$$

where  $\varepsilon_{PI}$  and  $\varepsilon_{UV}$  are the absorption coefficient of the photoinitiator and UV dopant, respectively, and  $l$  is the travel distance of the photon scattered from the last particle. Once absorption occurs, the portion of the photon energy absorbed by the photoinitiator is calculated as an input for the photopolymerization reaction.

TABLE II. Numerical parameters.

Gaussian radius	$w_0 = 4 \times 10^{-6}$ m
Monomer initial concentration	$4.46 \times 10^3$ mol/m <sup>3</sup>
Density of HDDA	$\rho = 1.01$ kg/m <sup>3</sup>
Photoinitiator initial concentration	$2.23 \times 10^2$ mol/m <sup>3</sup>
UV absorber initial concentration	7.31 mol/m <sup>3</sup>
Quantum yield	$\psi = 0.2$
Molar absorptivity of photoinitiator	$\epsilon_{PI} = 20.0$ m <sup>2</sup> /mol
Molar absorptivity of UV absorber	$\epsilon_{UV} = 20\,000.0$ m <sup>2</sup> /mol
Refractive index of HDDA	1.4
Refractive index of ceramic powder	1.7
Laser wavelength	364 nm
Radius of ceramic powders	0.5 $\mu$ m

Steps 3 and 4 are repeated until the photon is absorbed, which ends the tracing of one photon packet. 10<sup>6</sup> photon packets are calculated in this simulation to achieve accuracy.

**B. Microscale photo polymerization**

Once the light absorption profile is determined by the above procedures, a set of differential equations are used to simulate the photopolymerization process<sup>21</sup>

$$\begin{aligned} \text{Attenuation of light} \quad & \frac{dI}{dz} = -\epsilon[S]I, \\ \text{Photo-initiation} \quad & \frac{d[S]}{dt} = -\psi\epsilon[S]I, \\ \text{Propagation} \quad & \frac{d[M]}{dt} = -k_p[R\cdot][M], \\ \text{Termination} \quad & \frac{d[R\cdot]}{dt} = \phi\epsilon[S]I - k_t[R\cdot]^2, \end{aligned}$$

where  $I$  is the light intensity,  $\epsilon$  the molar absorption of radicals,  $k_p$  the rate constant of propagation reaction, and  $k_t$  the rate constant of termination reaction. The variables  $[S]$ ,  $[R\cdot]$ , and  $[M]$  are the concentration of photoinitiators, radicals, and monomers, respectively.  $\psi$  is the quantum yield that determines the number of photoinitiator molecules photolyzed by every actinic photon. Under room temperature, the two rate constants  $k_p$  and  $k_t$  are obtained from the literature.<sup>21,22</sup> Percentage of monomer conversion is used as a measure of the polymerization in the model.<sup>14</sup> Through calculating concentration changes in the photoinitiator, radical, and monomer, this model simulates photopolymerization. Numerical simulation parameters are listed in Table II.

**EXPERIMENT**

Experiments on curing depth and curing radius are designed to compare numerical results. As shown in Fig. 6, a quartz window, which is UV transparent, is placed on the top of the ceramic suspension. Spacers are then placed between the quartz window and the silicon substrate to maintain a fixed 500  $\mu$ m thickness of ceramic suspension. Next, a laser beam with a given intensity is focused onto the upper surface of the ceramic suspension confined by the quartz window. By changing the duration of laser exposure, various optical doses can be obtained. After laser exposure, the solidified “cone-shaped” dots are attached to the quartz window.

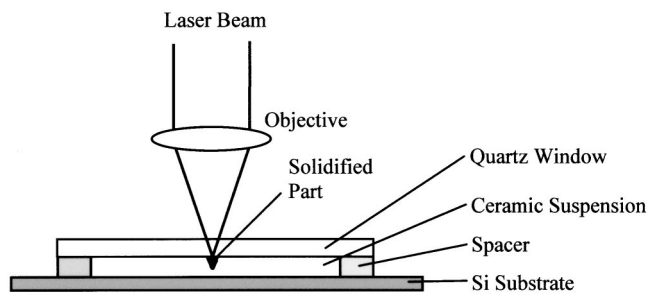


FIG. 6. Schematic diagram of curing depth and curing radius experiment setup.

Deionization water is used after exposure to remove the unpolymerized ceramic mixture. The curing depth and radius of the solidified dots on the quartz window are measured by an optical microscope. The ceramic suspension has 57% solid loading and is mixed with a 0.3% UV absorber. For comparison, the numerical simulations are performed at the same conditions.

**RESULTS AND DISCUSSION**

The calculated intensity profile of light propagating within the resin is shown in Fig. 7. The incident light is perpendicularly illuminated on the resin surface. The attenuation of the light intensity is observed along with the  $z$  dimension due to absorption and scattering. The intensity profiles are typically bulletlike, which mainly result from the initial distribution of the incident light and the light scattering during light propagation.

A simulated shape of the solidified part from a single exposure at a fixed position is shown in Fig. 8. The bulletlike shape is similar to the shape observed from experiments. While a similar bulletlike shape is also computed in laser polymerization of pure polymer resin at the same exposure conditions, the solidified cone from ceramic suspension has a larger diameter and a smaller depth.

The result demonstrates that the light scattering does indeed influence the shape of the fabricated part. The ceramic

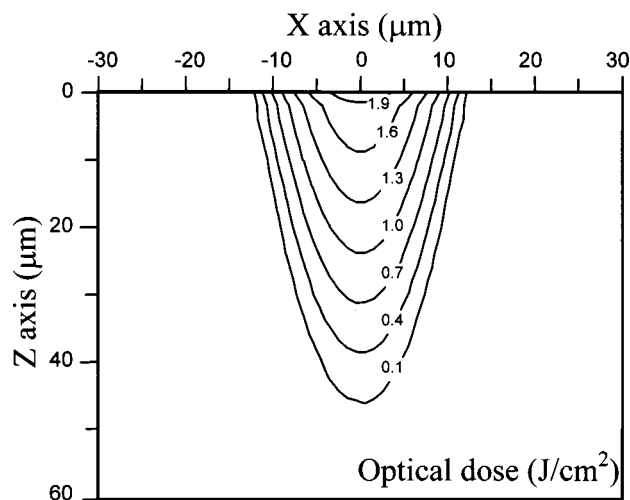


FIG. 7. Optical dose profile of light propagating within the UV curable resin. The optical dose at resin surface is 2 J/cm<sup>2</sup>.

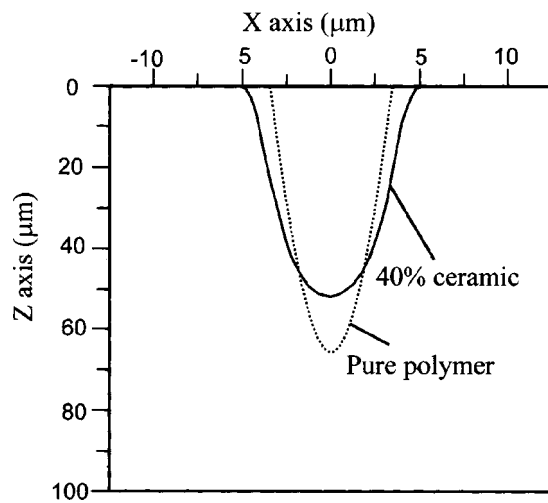


FIG. 8. Simulated shapes of the solidified parts for pure polymer and ceramic suspension (40% solid loading), respectively. Laser intensity is  $5.0 \times 10^4 \text{ W/m}^2$ , exposure time is 0.5 s.

particles scatter the incoming photons, which are initially perpendicularly shot into suspension. Thus, the scattered photons travel laterally into the surrounding area instead of penetrating into the depth direction. Consequently, the final solidified parts present a larger diameter and a shorter depth.

Curing depth and curing radius are two important parameters that directly determine the spatial resolution, as well as overall dimensional control in stereolithography.<sup>3,23</sup> Smaller curing depth and radius usually give better fabrication resolution. However, if the curing depth is shorter than the designed layer thickness, the adhesion between layers can be poor. Therefore, optimization of process parameters for curing depth and curing radius is critical in the  $\mu\text{SL}$  fabrication. This numerical simulation is carried out to understand how the process parameters influence the curing depth and curing radius in the microscale light scattering and photopolymerization.

Figure 9 shows the curing depth and radius dependences on laser intensity for a 40% solid loading ceramic suspension. Both parameters grow as the laser intensity increases; the curing depth changes from 66 to 90  $\mu\text{m}$ , and the curing

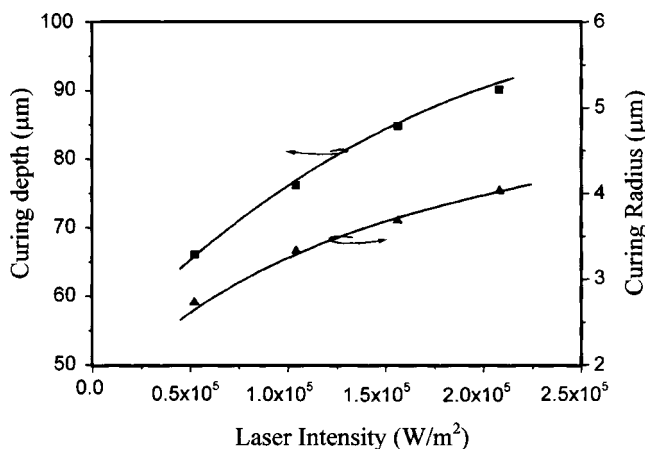


FIG. 9. Curing radius and curing depth dependence on the laser intensity at solid loading of 40%, exposure time of 0.5 s, and doping level of 0.3%.

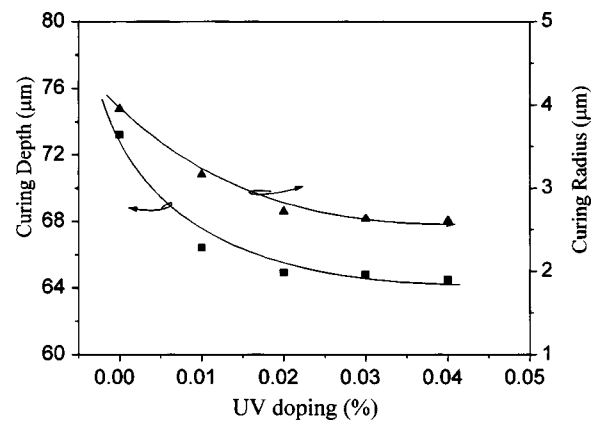


FIG. 10. Curing radius and curing depth dependence on UV doping at solid loading of 40%, laser intensity of  $0.5 \times 10^5 \text{ W/m}^2$ , and exposure time of 0.5 s.

radius changes from 2.7 to 4  $\mu\text{m}$ , as the laser intensity increases from  $0.5 \times 10^5$  to  $2 \times 10^5 \text{ W/m}^2$ . With the increased number of incoming photons, more photons are scattered to the surrounding area to induce the polymerization, which makes the size of the solidified cone bigger. It is observed that the microcone structure with an aspect ratio of 10:1 can be created by ceramic  $\mu\text{SL}$ , which demonstrates a unique capability for a high-aspect ratio microfabrication in a single-laser scan. This has been demonstrated in the experiment. However, this observation also presents a challenge in curing depth control, which is critical in the fabrication of microstructures with complex contours.

A unique UV doping technique has now been developed which decreases the curing depth and curing radius by absorbing the scattered laser light.<sup>16</sup> In this technique, the doping effect in  $\mu\text{SL}$  of ceramics is examined by the numerical simulation. Figure 10 shows the dependences of the curing depth and the curing radius of solidified microcone on the UV doping. This numerical simulation reveals that both curing depth and curing radius decrease with the increase of the UV doping level. By increasing the UV dopant concentration from 0% to 0.4%, the curing depth drops from 73 to 64  $\mu\text{m}$ , and the curing radius shrinks from 4 to 2.6  $\mu\text{m}$ .

This result suggests that UV doping can effectively improve the spatial resolution of the ceramic  $\mu\text{SL}$ . With increases of the UV doping level, more scattered photons will be absorbed by UV dopants, limiting photopolymerization reactions both in depth and lateral dimension. Under the same laser intensity, one can fabricate a smaller feature-sized ceramic  $\mu\text{SL}$  with a higher-UV doping level.

Experiments are also conducted to compare the numerical simulations with doping effects (Fig. 11). The monomer resin is mixed with 57% ceramic powders (volume ratio) and 0.3% UV absorber. This experiment revealed that when the laser intensity is increased from 40 to 240  $\text{W/cm}^2$ , the curing depth increases from 18 to 34  $\mu\text{m}$ , and curing radius increases from 10 to 14  $\mu\text{m}$ . Comparatively, the numerical study shows that the curing depth increases from 23 to 36  $\mu\text{m}$ , and the curing radius increases from 9 to 14  $\mu\text{m}$ . The numerical simulations are in good agreement with the experimental results. The maximum differences of numerical

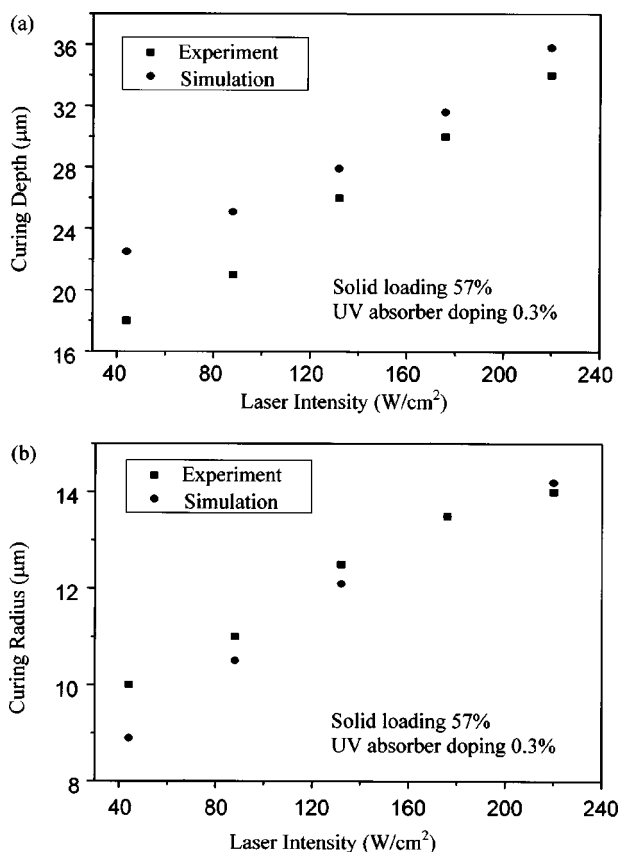


FIG. 11. Numerical and experimental results of (a) curing radius vs laser intensity and (b) curing depth vs laser intensity. The laser exposure time is 0.5 s.

and experimental results of curing depth and curing radius are within 5 and 1  $\mu\text{m}$ , respectively, which is within 25% of the value.

There are some interesting characteristics in numerical and experimental values. First, the numerical and experimental differences are relatively larger at the lower-laser intensity. Second, the experimental curing depth is smaller than numerical values, while the experimental curing radius is larger than numerical values. This may be due to some secondary effects resulting from the assumptions made in the modeling.

Further investigation is made to study the dependence of the focused laser beam radius on the curing radius by using the numerical model (Fig. 12). The results reveal that as the curing radius reduces from 8 to 2.6  $\mu\text{m}$ , the fabrication achieves an enhanced resolution along with the focused laser spots' dimensions reducing from 5 to 0.25  $\mu\text{m}$ . It should be noted that nonlinear dependence has been observed when a laser beam spot is focused on a dimension smaller than 2  $\mu\text{m}$ . The ultimate fabrication resolution of 2.6  $\mu\text{m}$  in ceramic microstereolithography is found when the focused beam's radius reaches the diffraction limit of about 0.25 micron. The significant broadening of the curing width at this diffraction limit is largely due to the light scattering and subsequent photochemical polymerization.

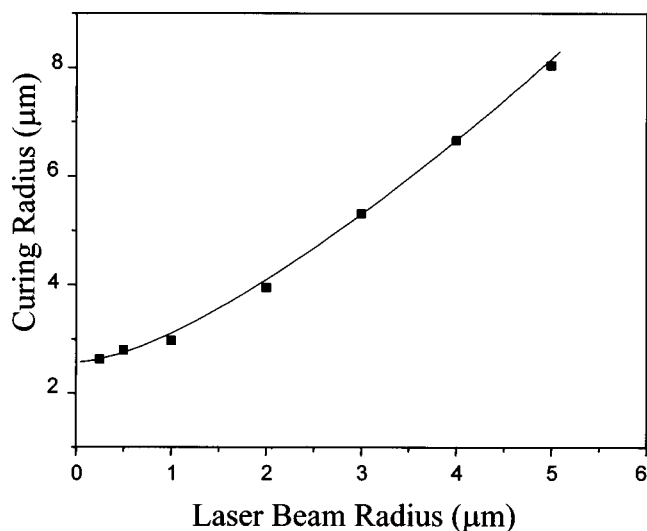


FIG. 12. The curing radius dependence of the focused beam spot radius.

## CONCLUSION

In this work, both the experimental method and numerical modeling were used to investigate ceramic microstereolithography. The Monte Carlo ray-tracing method was developed to simulate light absorption and scattering in concentrated ceramic suspensions, while the subsequent photoinduced polymerization was simulated by the finite difference method. The influence of critical process parameters were studied through the developed numerical model. Light scattering was found to significantly increase the fabricated feature width, and therefore, degrade the fabrication precision.

In addition, a UV doping technique was also developed to enhance the fabrication precision by reducing the light scattering. In this study, the experimental measurements of curing depth and curing width are found to be in good agreement with the numerical modeling. The ultimate fabrication precision of 2.6  $\mu\text{m}$  is predicted by the numerical model.

## ACKNOWLEDGMENTS

This work was supported by the Office of Naval Research under Contract Nos. N00014-01-1-0803 and N00014-02-1-02240 and the National Scientific Foundation, Award No. DMI-0196395.

<sup>1</sup>A. B. Frazier, R. O. Warrington, and C. Friedrich, *IEEE Trans. Ind. Electron.* **42**, 423 (1995).

<sup>2</sup>H. Fujita, *Proc. IEEE* **86**, 1721 (1998).

<sup>3</sup>P. F. Jacobs, *Rapid Prototyping and Manufacturing: Fundamentals of Stereolithography* (Society of Manufacturing Engineers Publishers, Dearborn, 1992).

<sup>4</sup>M. L. Griffith and J. W. Halloran, *J. Am. Ceram. Soc.* **79**, 2601 (1996).

<sup>5</sup>D. L. Bourell, H. L. Marcus, J. W. Barlow, and J. J. Beaman, *Int. J. Powder Metall.* **29**, 369–381 (1992).

<sup>6</sup>S. C. Danforth and A. Safari, *10th IEEE International Symposium on Applications of Ferroelectrics* (IEEE, Piscataway, NJ, 1996), pp. 183–188.

<sup>7</sup>E. Sachs, M. Cima, J. Bredt, A. Curodear, T. Fan, and D. Brancazio, *Manuf. Rev.* **5**, 117 (1992).

<sup>8</sup>E. A. Griffin, D. R. Mumm, and D. B. Marshall, *Am. Ceram. Soc. Bull.* **75**, 65 (1995).

- <sup>9</sup>M. L. Griffith and J. W. Halloran, *ASME J. Manuf. Sci. Eng.* **2**, 529 (1994).
- <sup>10</sup>K. Ikuta and K. Hirowatari, *IEEE Micro Electro Mechanical Systems: An Investigation of Micro Structures, Sensors, Actuators, Machines and Systems* (IEEE, Piscataway, NJ, 1993), pp. 42–47.
- <sup>11</sup>T. Nakamoto, K. Yamaguchi, P. A. Abraha, and K. Mishima, *J. Micro-mech. Microeng.* **6**, 240 (1996).
- <sup>12</sup>X. Zhang, X. N. Jiang, and C. Sun, *Sens. Actuators A* **77**, 149 (1999).
- <sup>13</sup>S. Maruo and S. Kawata, *J. Microelectromech. Syst.* **7**, 411 (1998).
- <sup>14</sup>S. Maruo and K. Ikuta, *International Symposium on Micromechatronics and Human Science* (IEEE, Piscataway, NJ, 1998), p. 173.
- <sup>15</sup>G. Odian, *Principles of Polymerization* (McGraw-Hill, New York, 1970).
- <sup>16</sup>X. Zhang and C. Sun (to be published).
- <sup>17</sup>H. C. van de Hulst, *Light Scattering by Small Particles* (Wiley, New York, 1957).
- <sup>18</sup>M. L. Griffith and J. W. Halloran, *J. Appl. Phys.* **81**, 2538 (1997).
- <sup>19</sup>H. M. Liao and T. W. Coyle, *J. Can. Ceram. Soc.* **65**, 254 (1996).
- <sup>20</sup>Y. M. Govaerts and M. Verstraete, *IEEE Trans. Geosci. Remote Sens.* **36**, 493–505 (1998).
- <sup>21</sup>J. Wen, Master thesis, Pennsylvania State University, PA 1998.
- <sup>22</sup>G. R. Tryson and A. R. Shultz, *J. Polym. Sci., Polym. Phys. Ed.* **17**, 2059 (1979).
- <sup>23</sup>X. N. Jiang, C. Sun, X. Zhang, B. Xu, and Y. H. Ye, *Sens. Actuators A* **87**, 72 (2000).